

# Fuzzy logic gain-tuned adaptive second-order GI-based multi-objective control for reliable operation of grid-interfaced photovoltaic system

ISSN 1751-8687

Received on 6th July 2017

Revised 18th October 2017

Accepted on 28th October 2017

E-First on 19th January 2018

doi: 10.1049/iet-gtd.2017.0958

www.ietdl.org

Srinivas Vedantham<sup>1</sup> ✉, Shailendra Kumar<sup>1</sup>, Bhim Singh<sup>1</sup>, Sukumar Mishra<sup>1</sup>

<sup>1</sup>Department of Electrical Engineering, IIT Delhi, New Delhi 110 016, India

✉ E-mail: vlsrinivas16@gmail.com

**Abstract:** This study presents the fuzzy logic integrator gain-tuned improved second-order generalized integrator (GI) for a double-stage grid-interfaced photovoltaic (PV) system. The proposed system includes the functionalities of feeding active power to the grid, power factor correction, grid currents balancing and system isolation under grid side faults. Moreover, the smooth system operation is ensured under weak distribution grids where grid voltage is subject to huge diversions. Furthermore, automatic protection scheme for the system under grid-side faults is also established with the proposed algorithm for increased reliability. The fuzzy-tuned GI provides advantages of efficient and effective extraction of load current fundamental component under steady-state and dynamic grid conditions. The non-linear frequency error variation is compensated here using fuzzy logic-based self-tuning integrator gain of the controller. The controller is improved to mitigate the possible DC component in the load current. The neutral current in the loads is nullified by using a four wire system. The adaptive DC bus voltage helps to minimize the switching losses and prevents unexpected tripping of the PV inverter. The system is experimentally verified using a prototype built in the laboratory.

## 1 Introduction

Increased demand for electric energy has been exhibited in the recent years. According to the US energy information administration (EIA) Historical Statistics for 2014, the electricity generation worldwide has been 22,433 TWh. This has been increased to 23,930 TWh in 2015 [1]. Owing to high-energy demand and depletion of non-renewable energy sources as oil, coal and natural gas, increased dependency on renewable energy sources has been marked over past few years [2, 3]. Of late, the distributed energy sources, which include solar energy, wind energy, bio-gas energy emerged as the prominent energy sources, out of which a significant usage of solar energy for domestic and industrial applications has been exhibited [4].

A three-phase single-stage grid-interfaced photovoltaic (GPV) system with one cycle control (OCC) has been proposed in [5]. This type of control can be implemented digitally and is based on current source inverter topology [6]. This control waives off the services of digital signal processor (DSP). Owing to simplicity in design, OCC-based single-phase systems are implemented; however, it needs systematic tuning to enhance the power output for different solar insolation levels [7]. Moreover, in cloudy days or night times, the solar voltage-source converter (VSC) could be used as active compensator. Kuo *et al.* in [7] have discussed active power filtering in cloudy days for single-phase solar PV system using 3-leg VSC. The single-stage GPV system topologies are discussed in [8] along with their comparison and it has been noted that standard VSC topology possesses lowest losses with acceptable total harmonic distortion (THD) under IEEE standards. A multilevel topology for GPV systems is introduced in [9], where the steps voltage waveforms are produced by a good space vector pulse-width modulation technique, which is acceptable for the real-time execution in industrial digital signal processors.

The grid integration of solar PV system for injecting active power to the grid has been contemplated in the literature [10, 11] with various functionalities. The power quality improvement features with GPV systems have been addressed in [12]. The synchronous reference frame theory (SRFT)-based control algorithm has been developed in [13]. The control approach supports zero-voltage regulation and reactive power compensation

features. However, it suffers with dynamic response due to the problem of presence of low-pass filter for reference extraction. Moreover, the steady-state response is hampered during unbalanced load perturbations, by setting large cut-off frequency accounting for the dominant second harmonic component in the  $d$ -axis current. Thus, a trade-off is observed at all times to compromise either steady-state or dynamic responses. Moreover, control algorithm robustness is affected by dependency on phase locked loop (PLL). To overcome these drawbacks, a notch filter-based algorithm has been developed in [14]; nonetheless, the ideal amplitude and ideal phase characteristics of notch filter make it difficult to implement in the real time. The improved linear sinusoidal tracer (ILST)-based algorithm [15] suffers poor steady-state response, since a low pass filter (LPF) is present in the path of fundamental extraction. To address the aforementioned difficulties, least mean fourth (LMF)-based control scheme has been reported in [16], yet the algorithm suffers stability issues as its stability depends on input signal power and initialisation weights. Moreover, there is always a trade-off for selecting adaptation constant of the algorithm to attain fair steady-state and dynamic responses, due to it being a linear adaptive filter.

The generalised integrator (GI)-based algorithms such as second-order GI (SOGI), with and without frequency LL (FLL), suffer the disadvantages of lack of frequency estimation and lack of DC offset rejection capability, respectively. The improved efforts are being made for optimal switching of VSC to obtain fast, reliable and flexible GPV system. The fuzzy logic tuning of SOGI facilitates adaptive variation in integrator gain leading to accurate and smooth frequency estimation of in-phase and quadrature fundamental components of load current during system frequency perturbation.

The non-linear behaviour of system frequency error variation is linearised in conventional SOGI. The adaptive integrator gain tuning using fuzzy logic, accounts for non-linear behaviour in frequency error variation characteristics. The complexity of proposed improved SOGI-FLL (ISOGI-FLL) is low as compared with the aforementioned control methods. The adaptive gain for estimation of system frequency facilitates smooth steady-state response and fast convergence under dynamic conditions. The

ISOGI to remove the DC offset components in load currents is reported in the literature [17]. The present paper proposes an ISOGI-based FLL with integrator gain-tuned using fuzzy logic for three-phase four wire GPV system. The four wire GPV system is used to compensate load neutral current to maintain zero grid neutral current for practical purposes. The salient features of the present work are as highlighted here:

- (i) As the load currents are processed in independent manner, the control scheme is phase independent.
- (ii) Good frequency characteristics are observed with less complexity. During faults in the system, frequency-dependent-based algorithm is more stable in comparison of phase angle of voltage.
- (iii) The effectiveness in DC offset filtering capabilities from the non-linear load current to extract the fundamental component is demonstrated by frequency response analysis. Moreover, the frequency tracking characteristics of the proposed control scheme is demonstrated with respect to SO integrator-based control.
- (iv) Adaptive DC-link voltage variation reduces the converter losses and avoids VSC tripping under weak distribution grid conditions. The experimental results depicting adaptive nature of DC bus voltage are presented. Moreover, the PV feed-forward term helps to improve the dynamic response.
- (v) The grid neutral current is nullified by deploying four-leg VSC for reliable operation of power equipment in practical power systems.
- (vi) For an increased reliability, PV-VSC system protection under grid-side faults is established by the proposed controller.

A laboratory prototype has been developed and the corresponding experimental results validate the performance of the proposed controller. The satisfactory system behaviour is observed and the THDs in the grid currents are maintained within the limits set by an IEEE-519 standard [18].

## 2 Three-phase four wire GPV system configuration

Besides the PV array, the proposed GPV system includes a boost converter for maximum power extraction, a four-leg VSC with a DC-link capacitor ( $C_{DC}$ ), an interfacing inductor ( $L_f$ ) and a ripple filter. The configuration of proposed system is presented in Fig. 1a. The interfacing inductor eliminates the ripples in grid current while the ripple filter at point of common coupling (PCC) absorbs high-frequency switching noise produced by the VSC. The control scheme is realised through current reference control of VSC gating pulses. The neutral current injected by the non-linear loads in a practical system is compensated through appropriate gating pulses to the fourth leg of VSC. A prototype of proposed system is developed in the laboratory and the system is tested under both steady-state and dynamic test conditions.

## 3 Control approach

The maximum power extraction from the solar PV array is ascertained by an incremental conductance (InC)-based maximum power point tracking (MPPT) strategy [19]. The InC-based MPPT algorithm carries its own advantages [20, 21], while holding a few disadvantages [20]. The gating pulses generation for DC-DC boost converter to achieve MPPT is presented in Fig. 1b. The InC algorithm, therefore, estimates the reference PV array voltage ( $V_{pv}^{ref}$ ). The duty ratio is obtained from the reference PV array voltage and DC-link voltage as

$$d_{Boost}^{ref} = \begin{cases} 1 - \frac{V_{PV}^{ref}}{V_{DC}} & \text{If } v_{grid} > v_{grid,min} \\ 0 & \text{Otherwise} \end{cases} \quad (1)$$

The duty ratio obtained from (1) is compared with high-frequency carrier signal (10 kHz) to produce switching pulses to the boost converter. However, the duty ratio for the boost converter is made

zero, as soon as the grid voltage dips below minimum grid voltage ( $v_{grid,min}$ ) in any of the phase indicating the occurrence of the grid-side fault and the PV system, therefore, needs to be isolated for protection purpose. The gating pulses for four-leg VSC switches are generated using FLL-based ISOGI algorithm with fuzzy logic-based self-tuned integrator gain.

### 3.1 ISOGI algorithm with fuzzy logic-based self-tuned integrator gain

The fuzzy logic (FL) control-based ISOGI algorithm estimates the fundamental power-consuming component of load current for the three phases. The input load current ( $i_L$ ) is filtered from harmonics and quadrature shift from the fundamental component ( $i_{LaQ}$ ) of load current is the output by the algorithm. Thus, the transfer function of SOGI-Q-based algorithm can be evaluated as [22]

$$F_1(s) = i_{LaQ}(s)/i_L(s) = \alpha\omega_1^2/(s^2 + \alpha\omega_1s + \omega_1^2) \quad (2)$$

Here, ' $\omega_1$ ' represents the fundamental frequency and ' $\alpha$ ' is the characteristic parameter that determines the filter bandwidth. The ISOGI-based algorithm provides good DC offset rejection capability than conventional SOGI-based algorithm. The structure of ISOGI-based control scheme is highlighted in Fig. 1c. The in-phase component ( $i_{LaD}$ ) and quadrature component ( $i_{LaQ}$ ) of fundamental of load current are shown in Fig 1c. The transfer functions corresponding to fundamental quadrature component [ $i_{LaQ}$ ] and error signal ( $e_{La}$ ) of the algorithm can be identified as

$$Q(s) = \frac{i_{LaQ}(s)}{i_{La}(s)} = \frac{\alpha_1\omega^2s}{s^3 + (\alpha_1 + \alpha_0)\omega s^2 + \omega^2s + \alpha_0\omega^3} \quad (3)$$

$$E(s) = \frac{e_{La}(s)}{i_{La}(s)} = \frac{s(s^2 + \omega^2)}{s^3 + (\alpha_1 + \alpha_0)\omega s^2 + \omega^2s + \alpha_0\omega^3} \quad (4)$$

In (3) and (4), ' $\alpha_1$ ' is the characteristic parameter of ISOGI,  $\alpha_1 = 2\xi$ ,  $\xi$  is the under-damping factor where typically 0.707 [23], where ' $\alpha_0$ ' is the characteristic parameter determining the DC offset rejection. The relationship between the characteristic parameter ' $\alpha_1$ ' and ' $\alpha_0$ ' for a stable system is depicted in [17], given as

$$\alpha_0^3 + 3\alpha_1\alpha_0^2 + (3\alpha_1^2 + 9)\alpha_0 + \alpha_1^3 - 4.5\alpha_1 = 0 \quad (5)$$

Thus, the value of ' $\alpha_0$ ' can be identified as 0.27. Fig. 2a depicts the frequency response analysis of the ISOGI algorithm [i.e. frequency response corresponding to the transfer function,  $i_{LaQ}(s)/i_{La}(s)$ ]. Without FLL, the 'central frequency' (corresponding to the dashed vertical line in Fig 2a) is fixed and cannot be varied even under change in system frequency, which introduces an error in fundamental amplitude estimation of load currents. However, when the FLL depicted in Fig. 1c is introduced, the effective mechanism for adapting this central frequency is established.

The transfer functions for  $i_{LaQ}(s)$  and  $e_{La}(s)$  are depicted in (3) and (4), respectively. Fig. 2b illustrates Bode plot for the transfer functions  $E(s)$  and  $Q(s)$ . From the frequency response analysis (Fig. 2b), it can be observed that the signals  $i_{LaQ}$  and  $e_{La}$  are in-phase as long as the input frequency is lower than the fundamental frequency. However, the phase shift becomes 180° when the input frequency supersedes the fundamental frequency. For this reason, the products of  $i_{LaQ}$  and  $e_{La}$  can be defined as the frequency error ( $e_f$ ) as depicted in Fig. 1c. Thus, the frequency error would be positive when the input frequency is lower than the fundamental frequency, negative when the input frequency is greater than the fundamental frequency and zero otherwise.

Hence, an integral controller with negative gain ( $-\beta$ ) can be used to make the zero DC component of the frequency error by shifting the SOGI central frequency until matching input frequency. Thus, the input frequency is directly detected by the FLL as  $\dot{\omega} = -\beta i_{LaQ}e_{La}$ . This reduces frequency error to zero.



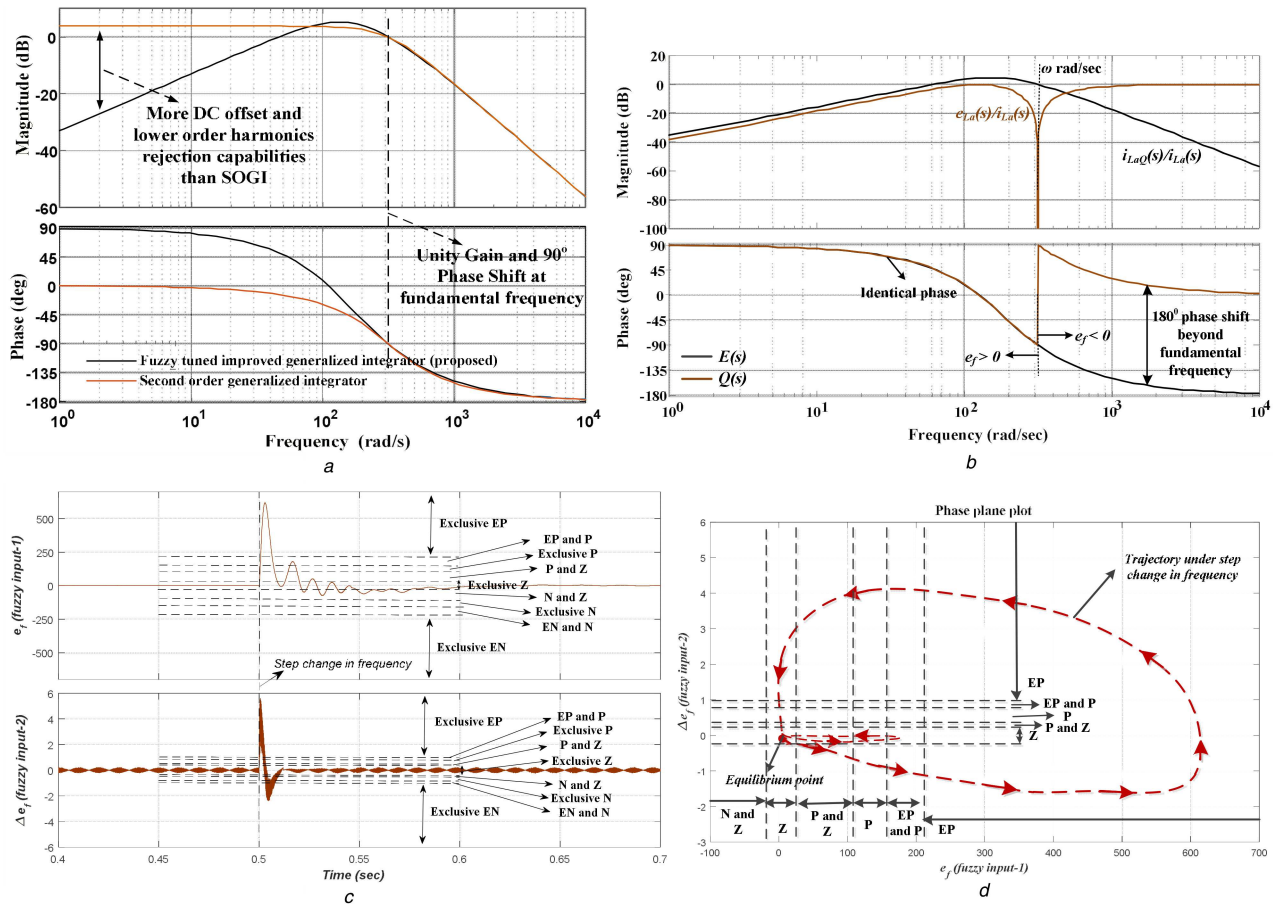


**Fig. 2** Frequency response and phase plane analysis of the system

(a) Frequency response of the proposed algorithm depicting the DC offset filtering capability, (b) Frequency response analysis of the FLC input variables ( $i_{LaQ}$  and  $e_{La}$ ). (c) Response of FLC inputs ( $e_f$  and  $\Delta e_f$ ) to step change in frequency (depicting various regions), (d) Phase plane plot of FLC inputs – trajectory under step change in frequency

tunes the gain ' $f_{out}$ ' which is input to FLL for proper frequency estimation. It uses frequency error and its derivative for this purpose. In Fig. 1c, the dotted arrows imply that the  $\omega$ -block of ISOGI inputs frequency from the estimated frequency ( $\omega_{estimated}$ ) computed using FLC.

The membership functions for fuzzy logic input–output relations comprise linguistic variables, namely extreme positive (EP), positive (P), zero (Z), negative (N) and extreme negative (EN), small (S), medium (M) and big (B). These functions are described in Fig. 1d. The grade of membership functions is acquired from

$$\psi(x) = 1 - |x - m|/0.5w \quad (7)$$

The coordinate corresponding to unity membership function is represented by ' $m$ '. The variables ' $x$ ' and ' $w$ ' represent value of input variable and width, respectively. Takagi-type fuzzy inference mechanism is used herein. Each of the rules is given weights ( $w_i$ ) according to the minimum operation given as

$$w_i = \min \{ \psi_{error}(e_f), \psi_{error}(\Delta e_f) \} \quad (8)$$

The weighted average of all rule outputs is estimated as variation of integral gain or fuzzy output ( $f_{out}$ ) as

$$f_{out} = \frac{\sum_{i=1}^N w_i z_i}{\sum_{i=1}^N w_i} \quad (9)$$

Here, ' $z_i$ ' represents the coordinate corresponding to respective output membership function and ' $N$ ' represents the number of fuzzy rules. The rules are listed in Table 1. The fuzzy inputs, i.e. frequency error and its derivative, are scaled by appropriate normalising factors ( $k_1$  and  $k_2$ ). The fuzzy-rule is expressed as

Rule: if  $e_f(k)$  is  $P_k$  and  $\Delta e_f(k)$  is  $Q_k$ , then  $f_{out}$  is  $R_k$ , where, ' $P_k$ ', ' $Q_k$ ' and ' $R_k$ ' are linguistic variables.

The basis for designing FLC rules (Table 1) can be explained in the following way. Consider, a step change in the system input frequency from '50' to '51 Hz' at 0.5 s. The response of fuzzy inputs, i.e. error ' $e_f$ ' and the change in error ' $\Delta e_f$ ' under this step variation in frequency is shown in Fig. 2c, along with various regions (EN, N, Z, P and EP). The corresponding phase plane plot is shown in Fig. 2d. The fuzzy logic rules in Table 1 are designed in accordance with the regions of fuzzy input depicted in Figs. 2c and d. In this case, for example, during the step change in frequency, input-1, i.e.  $e_f$  jumps to more than 500 and then gradually settles down to zero. During the time of high transients, i.e. 0.5–0.51 s, the fuzzy output ( $f_{out}$ ) has to be minimum value (i.e. S) in order to provide least multiplying factor ( $e_{La} \times f_{out}$ ) in FLL (Fig. 1c) and thus it provides high damping. Thus, accordingly, least or no oscillations are reflected in estimated frequency (the output of FLL). High transient in estimated frequency thus avoided by setting least or S output gain ( $f_{out}$ ) for high-transient inputs or inputs that fall in EP category. It can be noted that during high-transient period, the second input ( $\Delta e_f$ ) also goes higher into EP region. Therefore, either if ' $e_f$ ' goes high or ' $\Delta e_f$ ' goes high, the FLC has to output least gain ( $f_{out}$ ) to provide sufficient damping during dynamic performance/smooth dynamic response. Thus, the column corresponding to EP of input-' $e_f$ ' in Table 1 and the row corresponding to EP of input-' $\Delta e_f$ ' have  $f_{out} = S$ . Similar thing holds true for the column corresponding to EN of input-' $e_f$ ' in Table 1 and the row corresponding to EN of input-' $\Delta e_f$ ', i.e. FLC has to provide least gain ( $f_{out}$ ) for sufficient damping when the error ( $e_f$ ) or change in error ( $\Delta e_f$ ) shoots down in negative direction during frequency dip. This clarifies the first and last rows, columns in Table 1. Contrary to S gain which damps the input oscillations,

B output gain provides less damping but helps to reach steady-state quickly. Thus, the output gain ( $f_{out}$ ) is B for the case, where both  $e_f$  and  $\Delta e_f$  come under Z region. Moreover, for the same reason, B gain is necessary when either or both of two inputs ( $e_f$  and  $\Delta e_f$ ) come under P or N regions, to facilitate quick tracking of estimated frequency, and thus achieve steady-state quickly. However, when either of one input is in Z region but the other input is in P or N regions, the steady-state oscillations (situation where the output reaches the steady-state but oscillates for some time) are likely to happen, and therefore it is always safe to keep M output gain to avoid these unnecessary oscillations after reaching the steady-state; therefore, B output gain needs to be avoided in this situation. Thus, all the entries in Table 1 are covered hereby and the corresponding entries are justified.

### 3.2 Computation of unit templates

The sensed line voltages are converted to phase voltages ( $v_{sa}$ ,  $v_{sb}$  and  $v_{sc}$ ). The amplitude of PCC terminal voltage is estimated from phase voltages as

$$V_t = \sqrt{(2/3)(v_{sa}^2 + v_{sb}^2 + v_{sc}^2)} \quad (10)$$

The terminal voltage thus obtained is used to compute in-phase unit templates and quadrature unit templates as

$$[x_{pa} \ x_{pb} \ x_{pc}] = (1/V_t)[v_{sa} \ v_{sb} \ v_{sc}] \quad (11)$$

$$\begin{bmatrix} x_{qa} \\ x_{qb} \\ x_{qc} \end{bmatrix} = \frac{1}{2\sqrt{3}} \begin{bmatrix} 0 & -2 & 2 \\ 3 & 1 & -1 \\ -3 & 1 & -1 \end{bmatrix} \begin{bmatrix} x_{pa} \\ x_{pb} \\ x_{pc} \end{bmatrix} \quad (12)$$

### 3.3 DC-link voltage regulation

Unnecessary tripping of the converter and high VSC switching losses can be avoided by adapting the DC-link voltage reference in proportion to the terminal voltage ( $V_t$ ). Since the DC bus voltage is desired to be above the peak of the line voltage [24], the reference DC bus voltage can be defined as

$$V_{DC}^{ref} = \eta\sqrt{3}V_t \quad (13)$$

where ' $\eta$ ' is the safety factor. If the DC bus voltage reference is kept exactly equal to the peak of the line voltage, the additional voltage drop that occurs across the insulated gate bipolar transistor switches, interfacing inductor inductance and its internal resistance, do not get accounted. For this reason, the DC bus voltage reference must be kept at least little higher than the peak of the line voltage, as much as the additional voltage drop that occurs across the switches, the internal resistance and the interfacing inductors. Generally, this voltage drop is only 10–20% of peak line voltage. For this reason, a safety factor ' $\eta$ ' is included which is typically between 1.1 and 1.2. The sensed DC-link voltage is then compared with the reference DC bus voltage given by (13), and the error is passed through the proportional–integral (PI) controller. The output of the PI controller denotes the loss component ( $W_{ploss}$ ) which can be identified as

$$W_{ploss}(k) = W_{ploss}(k-1) + k_p\{V_{DCe}(k) - V_{DCe}(k-1)\} + k_i V_{DCe}(k)$$

**Table 1** Fuzzy logic rules

$\Delta e_f$	$e_f$					
	EN	N	Z	P	EP	
EN	$f_{out} = \mathbf{S}$					
N	$f_{out} = \mathbf{S}$	$f_{out} = \mathbf{B}$	$f_{out} = \mathbf{M}$	$f_{out} = \mathbf{B}$	$f_{out} = \mathbf{S}$	$f_{out} = \mathbf{S}$
Z	$f_{out} = \mathbf{S}$	$f_{out} = \mathbf{M}$	$f_{out} = \mathbf{B}$	$f_{out} = \mathbf{M}$	$f_{out} = \mathbf{S}$	$f_{out} = \mathbf{S}$
P	$f_{out} = \mathbf{S}$	$f_{out} = \mathbf{B}$	$f_{out} = \mathbf{M}$	$f_{out} = \mathbf{B}$	$f_{out} = \mathbf{S}$	$f_{out} = \mathbf{S}$
EP	$f_{out} = \mathbf{S}$					

$$(14)$$

where  $V_{DCe} = V_{DCref} - V_{DC}$  and  $k_p$ ,  $k_i$  are PI gains, respectively.

### 3.4 PV feed-forward compensation

A practical GPV system is prone to continuous perturbations in solar insolation. The dynamic response can be considerably improved under such continuous conditions by an additional feed-forward term computed using PV array power as

$$W_{pvff} = \frac{2P_{PV}}{3V_t} \quad (15)$$

### 3.5 Generation of VSC gating pulses

Thus, the quadrature fundamental component of load current ( $i_{Laq}$ ) obtained from the algorithm (Fig. 1c) is passed through sample and hold logic triggered from zero-crossing detector. The zero crossing of in-phase unit templates correspond to peak of quadrature fundamental component of the load current, and thus the amplitude of fundamental component of load currents ( $W_{pa}$ ,  $W_{pb}$  and  $W_{pc}$ ) are obtained. The average of fundamental component amplitude of three phases gives the equivalent weight component ( $W_{peq}$ ) of load current. The net active power-consuming weight component ( $W_{pnet}$ ) is then obtained as

$$W_{pnet} = W_{pL} + W_{ploss} - W_{pvff} \quad (16)$$

Reference grid currents for three phases are then evaluated utilising in-phase unit templates as

$$i_{sa}^* = \begin{cases} W_{pnet} \cdot x_{pa} & \text{if } v_{grid} > v_{grid, min} \\ 0 & \text{otherwise} \end{cases}$$

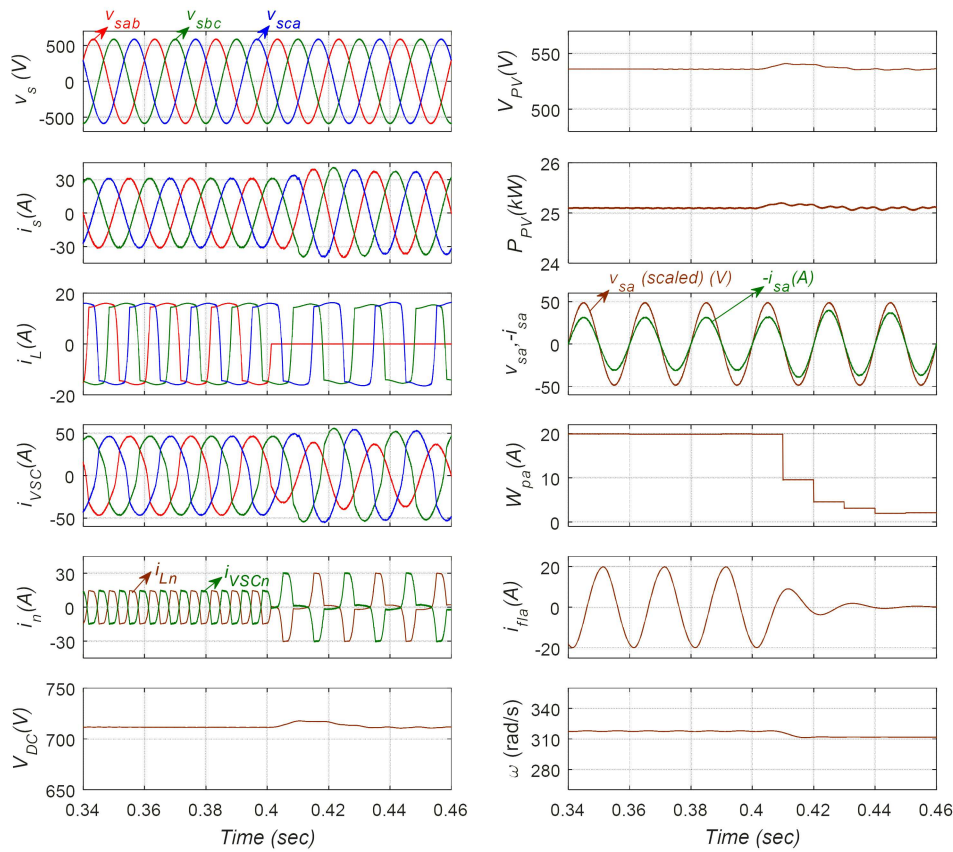
$$i_{sb}^* = \begin{cases} W_{pnet} \cdot x_{pb} & \text{if } v_{grid} > v_{grid, min} \\ 0 & \text{otherwise} \end{cases} \quad (17)$$

$$i_{sc}^* = \begin{cases} W_{pnet} \cdot x_{pc} & \text{if } v_{grid} > v_{grid, min} \\ 0 & \text{otherwise} \end{cases}$$

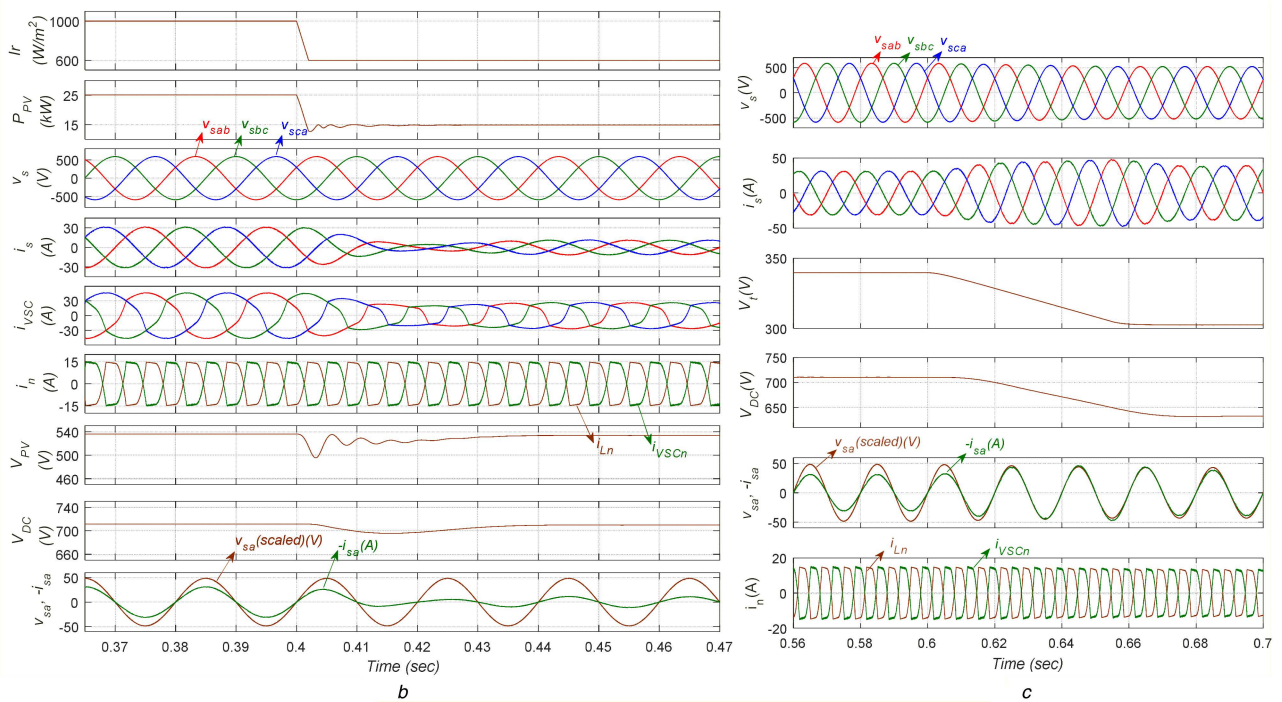
where  $v_{grid}$  refers to the grid three-phase voltages. As soon as any of the three-phase voltages becomes less than its minimum value ( $v_{grid, min}$ ), the reference grid current values are immediately adjusted to zero. This is set in order to avoid the over-currents through PV–VSC and grid-side equipment that occur during grid faults. Typically, it is safe to isolate the PV–VSC system if the grid-side voltages fall below 0.8 pu [25]. For this reason,  $v_{grid, min}$  can be considered 80% of nominal terminal voltage. The reference currents thus generated are compared with the sensed currents and the error is passed through the hysteresis current controller for generation of gating pulses to the three VSC legs corresponding to the three phases. The neutral grid current is computed from the summation of the three-phase grid currents as

$$i_{sn} = -(i_{sa} + i_{sb} + i_{sc}) \quad (18)$$

The pulses to the fourth VSC leg are generated from the hysteresis controller by comparing the reference neutral grid current (zero)



a



b

c

**Fig. 3** Simulation results under GPV system perturbations

(a) System response under load perturbation conditions, (b) GPV response under solar insolation change, (c) System performance for PCC voltage variations

with the grid neutral current computed from (18). The overall four-leg VSC control scheme is presented in Fig. 1b.

## 4 Simulation results

The proposed 3P4W system has been modelled and simulated in MATLAB<sup>®</sup>/Simulink-based environment for validation of fuzzy logic-based ISOGI-FLL algorithm. The solar PV is rated 25 kW. Simulation results depicting the situations of adaptive DC bus voltage, grid currents balancing and the dynamic performance

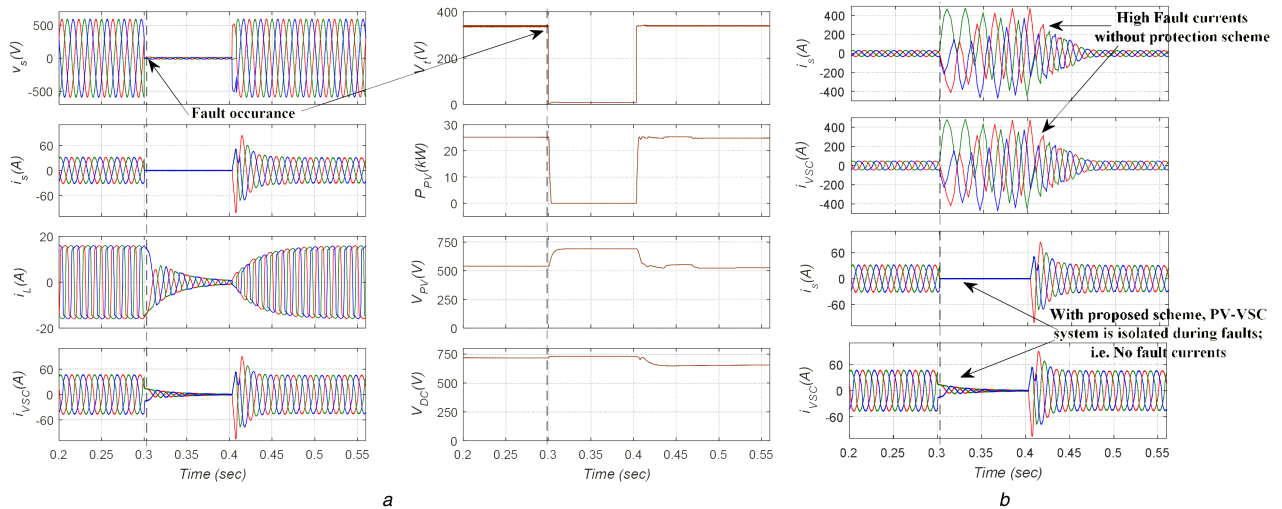
under non-linear load fluctuation and solar insolation change are highlighted in Fig. 3. The simulation parameters of the GPV system are reported in Table 2.

### 4.1 Performance under non-linear load unbalance and solar insolation variation

The GPV system feeding a non-linear load at PCC is subject to load unbalance at 0.4 s realised through disconnection of load in one of the phases. The performance and variation of system

**Table 2** Simulation system parameters

Parameter	Value	Parameter	Value
PV array power	25 kW	grid line voltage	415 V
PV module current	7.61 A	ripple filter	5 Ω, 10 μF
PV module voltage	26.3 V	interfacing inductor	6 mH
series modules	21	non-linear load	13 Ω, 400 mH
parallel modules	6	PI controller	$k_p = 0.9, k_i = 0.8$
DC-link capacitor	4700 μF	sampling time	10 μs
fuzzy input gains	$k_1 = 0.0064, k_2 = 0.005$	controller output gain	$\beta = 27.5$

**Fig. 4** System response under near PCC three-phase to ground fault

(a) Response of the system during grid-side fault (three-phase to ground), (b) Comparison of the system response under grid-side fault with (the proposed algorithm) and without minimum voltage imposition

parameters are depicted in Fig. 3a. The surplus power due to decrease in the load is fed to the distribution grid, and therefore the increase in grid currents is observed. Since the phase-'a' load has been disconnected, the corresponding decreases in its fundamental component ( $i_{f1a}$ ) and weight component ( $W_{pa}$ ) are observed.

The response of the system under solar insolation variation has been depicted in Fig. 3b. The solar insolation has been dropped from 1000 to 600 W/m<sup>2</sup> within timespan of 2 ms. Since the load consumption is same, the power fed back to the grid, and therefore the grid currents are expected to decrease.

#### 4.2 Performance under PCC voltage variation

As mentioned in the previous section, the adaptive DC-link voltage reference is used to reduce the converter switching losses. The system parameter variations under PCC voltage sag are illustrated in Fig. 3c. The DC bus voltage is observed to adapt as per the PCC voltage. Since the power fed from the solar PV array is the same, the decrease in PCC voltage has resulted in the increase of grid currents.

#### 4.3 Performance under grid-side faults

For a grid fault occurring at far-away point, there would be only a slight dip in the PCC voltage (for example, from 1 to 0.9 pu or so). In this case, the operation of the system continues with slight dip in the PCC voltage. The DC bus voltage reference adapts as (13) and the behaviour of the system under such slight voltage dips is depicted already in Fig. 3c.

However, for a fault occurring near to the PCC point, a considerable voltage dip can be noted within a very short span of time. The response of the system under such conditions is depicted in Fig. 4a. The most severe fault, i.e.: 'three phase to ground' fault with negligible fault resistance has been considered here at the PCC point. It can be inferred that the system, even under severe type of faults, is stable without any abnormal currents/voltages. Fig. 4b depicts comparison of the system response with the

proposed minimum voltage ( $v_{grid,min}$ ) imposition depicted in reference currents (17)/boost converter duty ratio (1) and without any grid minimum voltage imposition. Therefore, with the proposed control algorithm, reliability of the system is improved and automatic protection scheme for PV-VSC system and grid-side equipment is established.

#### 4.4 Effectiveness of the proposed control algorithm

The ability of the system to maintain unity power factor operation under load perturbation, solar insolation change and PCC voltage variation, has been illustrated in Figs. 3a-c, where the superimposed phase voltage ( $v_{sa}$ ) and negative phase current ( $-i_{sa}$ ) waveforms are presented, the phase voltage being scaled to one sixth for the sake of clarity. The neutral current compensation has also been illustrated Figs. 3a-c, where the solid line corresponding to the load neutral current ( $i_{ln}$ ) is compensated by the VSC neutral current ( $i_{vn}$ ) represented by the dotted line.

The comparative analysis of fuzzy-based control algorithm with the conventional SOGI-based control is demonstrated in Figs. 5a. The control performance under system frequency variation by 1 Hz is depicted in Fig. 5a. The linearisation of non-linear characteristic between the frequency error and central frequency is involved in conventional SOGI-FLL. The proposed fuzzy logic-based control solves the problem in linearisation of non-linear characteristics by adaptive tuning of the integrator gain, and therefore the steady-state performance is observed to be smooth. The dynamic performance, however, is also gradual and smooth without erroneous overshoot as depicted in Fig. 5a. The non-linear loads at PCC may contain various higher-order harmonic currents, and some of the loads may contain the DC offset which is removed to precisely track the fundamental component. An improved DC offset filtering capability of the proposed controller over SOGI is depicted in Fig. 2a. The comparative analysis of both the algorithms along with SRFT [13] and LMF [16] control schemes is highlighted in Table 3.

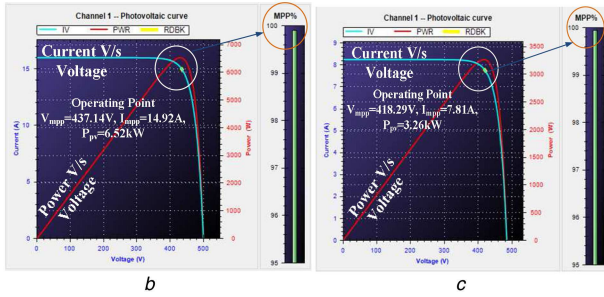
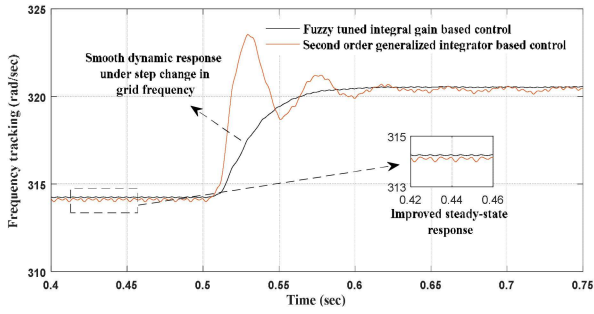


**Fig. 5** Comparative analysis of fuzzy-based control algorithm and the MPPT tracking performance

(a) Frequency tracking capability of the proposed algorithm compared with the conventional algorithm, (b), (c) MPPT performance at 1000 and 500 W/m<sup>2</sup>

## 5 Experimental results

A prototype of three-phase GPV system has been built in the laboratory. The solar PV array simulator (namely Ametek ETS600/17DVF) has been used for implementation of solar PV array-based power generation. The Hall-effect sensors are used for sensing line voltages and PV array voltage and sensing load currents, grid currents and the PV array current. The proposed control scheme is realised using DSP DSP-dSPACE1103. The opto-couplers are used to isolate DSP switching pulses and converter. The system response is recorded by using power analyser (Fluke 43-B) and digital storage oscilloscope (Agilent DSO714A). The performance of MPPT for the solar PV array simulator is presented in Figs. 5b and c, which assures that the MPP is being tracked under different solar insolation. The behaviour of proposed GPV system under various experimental conditions is illustrated in this section. The experimental system specifications are reported in Table 4.

### 5.1 Experimental behaviour of system parameters under load perturbation

To validate the performance of the proposed control, various intermediate signals are observed. These results are presented in Fig. 6 with respect to load perturbation. Fig. 6a highlights the extraction of unit templates ( $x_{pa}$ ,  $x_{pb}$ ,  $x_{pc}$ ). The variation of each phase weight component extraction ( $W_{pa}$ ,  $W_{pb}$ ,  $W_{pc}$ ) with load disconnection is presented in Fig. 6b. Fig. 6c depicts the variation of intermediate signals of controller, namely the  $\omega$  (rad/s) along with in-phase and quadrature components ( $i_{Lad}$  and  $i_{Laq}$ ). The net weight component ( $W_{pnet}$ ) along with loss component ( $W_{ploss}$ ), average weight component ( $W_{peq}$ ) and PV feed-forward component ( $W_{pvff}$ ) are shown in Fig. 6d. The final reference current extraction of all the three phases is presented in Fig. 7a. The in-phase and quadrature components ( $i_{Lad}$  and  $i_{Laq}$ ) and phase-‘a’ weight component drop to zero under load disconnection. The reference currents increase under load disconnection accounting for the extra power resulting from load disconnection being fed back to the grid.

The corresponding external signals are presented in Figs. 7b–d. The load currents ( $i_{La}$ ,  $i_{Lb}$ ,  $i_{Lc}$ ), phase-‘a’ VSC current and source current, solar PV array current ( $I_{PV}$ ) and DC bus voltage ( $V_{DC}$ ) along with source line voltage ( $v_{sab}$ ) are presented in Figs. 7b and

**Table 3** Comparative study of the control schemes

Parameter	Fuzzy logic tuned improved integrator (proposed)	FLL-based SOGI	SRFT [13]	LMF [16]
type	time-domain-based FLL	time-domain-based FLL	time-domain-based PLL	adaptive filter
complexity	low	low	high	low
frequency estimation	better	good	better	NA
DC offset filtering capability	high	low	NA	low
fundamental tracking accuracy	better	good	medium	poor
THDs in grid currents	low	medium	medium	high

**Table 4** Experimental system specifications

Parameter	Value	Parameter	Value
PV array current	16 A	PV array power	6.2 kW
ripple filter	6 $\Omega$ , 12 $\mu$ F	PV array voltage	500 V
DC-link capacitor	4700 $\mu$ F	non-linear load	1.5 kVA
interfacing inductor	3.5 mH	VSC rating	25 kVA
DSP sampling time	30 $\mu$ s	grid voltage	240 V

c. The load and VSC neutral current variations under load disconnection are depicted in Fig. 7d. The source neutral current is always maintained zero.

### 5.2 Test results under balanced non-linear load

Test results under balanced non-linear load are presented in Figs. 8 and 9. Figs. 8a–c present line voltage along with single-phase source current ( $i_{sa}$ ), load current ( $i_{La}$ ) and VSC current ( $i_{VSCa}$ ). The corresponding magnitudes are also highlighted. The neutral current compensation capability of the proposed control is presented in Figs. 9a–c. The grid power is shown negative justifying that the power is being fed to the grid. The THDs of source current and load current are presented in Figs. 8d and 9d, respectively. The THD of grid current is maintained at 3.8% despite the load current THD of 41.6%.

### 5.3 Response under unbalanced non-linear load

The experimental responses with phase-‘a’ load disconnection are presented in Figs. 10–12. The phase currents and neutral currents along with their magnitudes at source side, load side and at VSC are presented in Figs. 10a–d–12a–d, respectively. The displacement power factor of unity is realised at grid side. The utility currents are observed to be balanced despite unbalanced load and the grid neutral current remains zero. The neutral current compensation capability of the system has retained under load unbalance.

### 5.4 Experimental behaviour under solar insolation change

The GPV system is subject to solar insolation variation from 1000 to 500 W/m<sup>2</sup> and vice versa. The response in terms of PV array voltage ( $V_{PV}$ ), PV array current ( $I_{PV}$ ), VSC current ( $i_{VSCa}$ ) and source current ( $i_{sa}$ ) is depicted in Figs. 13a and b. The decrease in VSC and source currents is observed under solar insolation decrease accounting to reduced power being fed to the distribution grid.

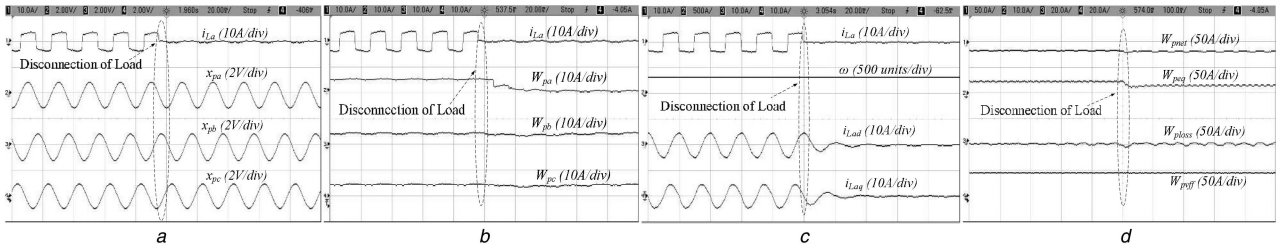


**Fig. 6** Dynamic performance for non-linear load perturbation  
 (a)  $i_{La}$  with  $x_{pa}$ ,  $x_{pb}$  and  $x_{pc}$ . (b)  $i_{La}$  with  $W_{pa}$ ,  $W_{pb}$  and  $W_{pc}$ . (c)  $i_{La}$  with  $\omega$ ,  $i_{Lad}$  and  $i_{Laq}$ . (d)  $W_{pnet}$  with  $W_{pavg}$ ,  $W_{ploss}$  and  $W_{pvff}$

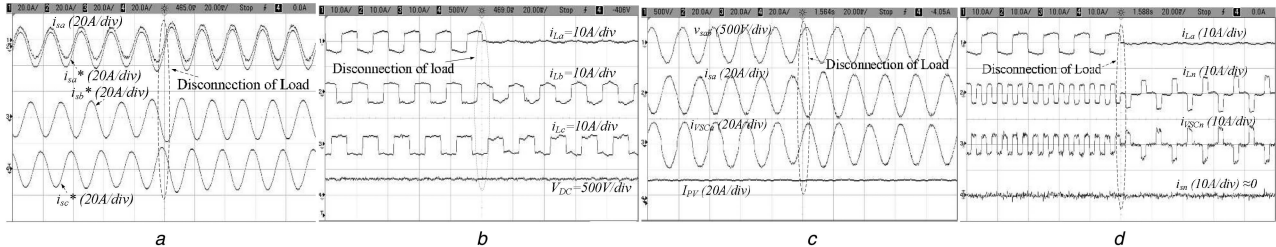


**Fig. 7** Dynamic response for non-linear load perturbation  
 (a)  $i_{sa}$  with  $i_{sa}^*$ ,  $i_{sb}^*$  and  $i_{sc}^*$ . (b)  $i_{La}$ ,  $i_{Lb}$ ,  $i_{Lc}$  and  $V_{dc}$ . (c)  $v_{sab}$ ,  $i_{sa}$ ,  $i_{vsc}$  and  $I_{pv}$ . (d)  $i_{La}$ ,  $i_{Ln}$ ,  $i_{vscn}$  and  $i_s$

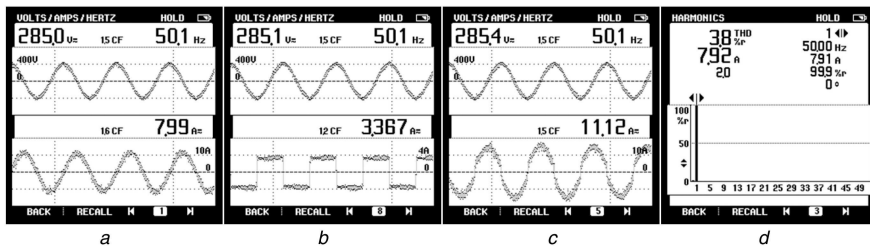


**Fig. 8** Test results under balanced non-linear load  
 (a)–(d)  $v_{sab}$  with  $i_{sa}$ ,  $i_{La}$ ,  $i_{vsc}$  and THD of  $i_{sa}$

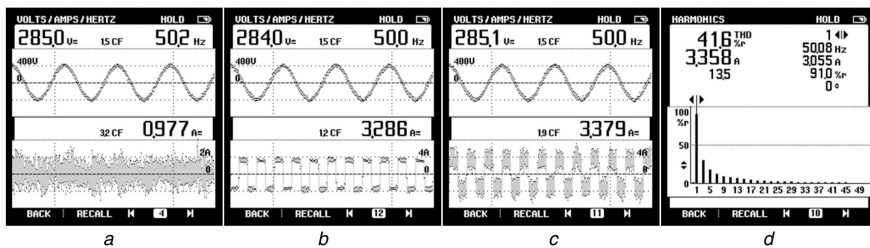


**Fig. 9** Test results for balanced non-linear load  
 (a)–(d)  $v_{sab}$  with  $i_{sn}$ ,  $i_{Ln}$ ,  $i_{vscn}$  and THD of  $i_{La}$

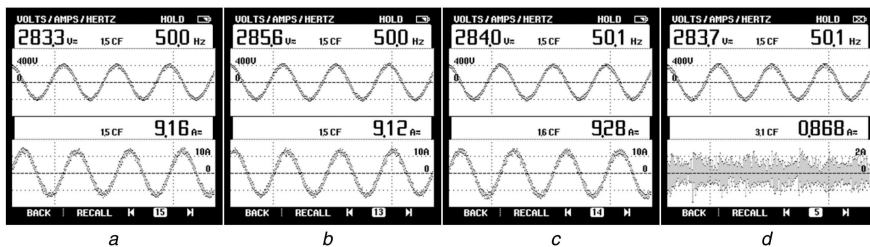


**Fig. 10** Test results under unbalanced non-linear load  
 (a)–(d)  $v_{sab}$  with  $i_{sa}$ ,  $i_{sb}$ ,  $i_{sc}$  and  $i_{sn}$

### 5.5 Experimental behaviour under PCC voltage fluctuations

The experimental validation under voltage sag at the grid side is carried out and the results are highlighted in Figs. 13c and d. The signals of grid currents ( $i_{sa}$ ,  $i_{sb}$ ,  $i_{sc}$ ), PV array current ( $I_{pv}$ ), DC bus voltage and PV array voltage ( $V_{pv}$ ) along with source voltage ( $v_{sab}$ ) are presented. The adaptive nature of DC-link voltage can be observed, while the PV array voltage and current remaining the

same. The increase in grid currents is observed accounting to the decrease of voltage at PCC, as the power fed to the grid remains unaffected.

## 6 Conclusions

The fuzzy logic gain-tuned improved SO integrator with FLL-based control strategy for the three-phase four wire GPV system is demonstrated with various functionalities. The non-linear

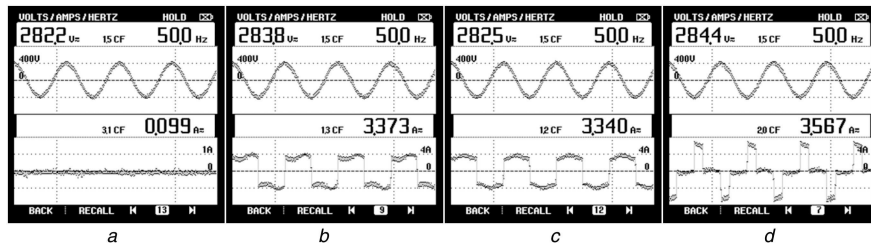


**Fig. 11** Test results for unbalanced non-linear load

(a)–(d)  $v_{sab}$  with  $i_{La}$ ,  $i_{Lb}$ ,  $i_{Lc}$  and  $i_{Ln}$

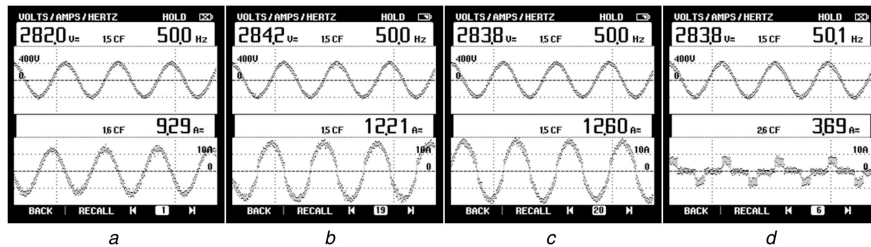


**Fig. 12** Test results of GPV under unbalanced non-linear loads

(a)–(d)  $v_{sab}$  with  $i_{VSCa}$ ,  $i_{VSCb}$ ,  $i_{VSCc}$  and  $i_{VSCn}$

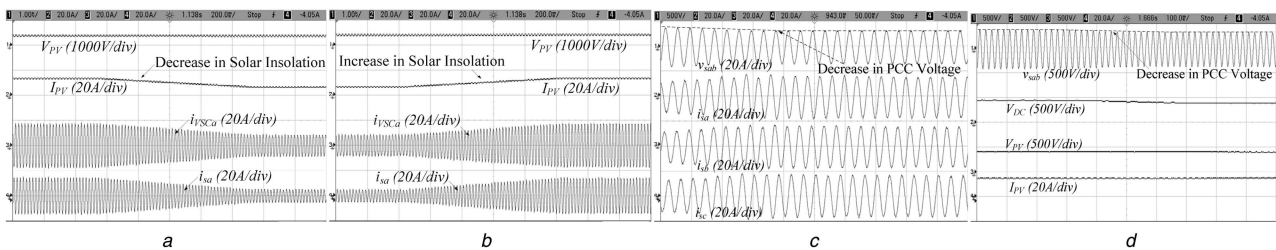


**Fig. 13** System response changes in solar irradiance and grid voltages

(a), (b) Dynamic performance for solar irradiance change (a) sudden reduction in insolation (b) increase in insolation, (c), (d) Response under reduction of PCC voltage from 400 to 340 V

behaviour of frequency error variation is linearised in conventional SOGI. The adaptive integrator gain tuning using fuzzy logic accounts for this non-linear behaviour and provides better convergence. The smooth frequency tracking and load current DC offset rejection capability of the proposed control have been demonstrated. The control algorithm is effective in fundamental component extraction and system frequency tracking. For reliable operation under weak distribution grids, where PCC voltages suffer huge diversions, the adaptive nature of DC-link voltage with respect to PCC voltage is also illustrated. Moreover, the system is proved reliable even under grid-side faults. The four-leg VSC control is able to mitigate the grid neutral current. Experimental results show the effectiveness of the algorithm under load unbalancing, power factor correction, variable solar insolation and PCC voltage sag and swell.

## 7 References

- [1] Kandpal, T.C., Broman, L.: 'Renewable energy education: a global status review', *Renew. Sust. Energy Rev.*, 2014, **34**, pp. 300–324
- [2] Vithayasrichareon, P., MacGill, I.F.: 'Valuing large-scale solar photovoltaics in future electricity generation portfolios and its implications for energy and climate policies', *IET Renew. Power Gener.*, 2016, **10**, (1), pp. 79–87
- [3] Tripathy, A.: 'Renewable energy at a glance', *Akshay Urja*, 2013, **6**, (5), p. 103
- [4] Dahlan, N., Jusoh, M., Abdullah, W.: 'Solar grid parity for Malaysia: analysis using experience curves', *IEEE Proc. Int. Conf. Power Engineering and Optimization*, 2014, vol. **24–25**, pp. 461–466
- [5] Fortunato, M., Giustiniani, A., Petrone, G., *et al.*: 'Maximum power point tracking in a one-cycle-controlled single-stage photovoltaic inverter', *IEEE Trans. Ind. Electron.*, 2008, **55**, (7), pp. 2684–2693
- [6] Chen, Y., Smedley, K.: 'Three-phase boost-type grid-connected inverter', *IEEE Trans. Power Electron.*, 2008, **23**, (5)
- [7] Kuo, Y., Liang, T., Chen, J.: 'A high-efficiency single-phase three-wire photovoltaic energy conversion system', *IEEE Trans. Ind. Electron.*, 2003, **50**, (1), pp. 16–122
- [8] Jain, C., Singh, B.: 'An adjustable DC link voltage based control of multifunctional grid interfaced solar PV system', *IEEE J. Emerg. Sel. Top. Power Electron.*, 2016, *early access*, 2017, **5**, (2), pp. 651–660
- [9] Grandi, G., Rossi, C., Ostojic, D., *et al.*: 'A new multilevel conversion structure for grid-connected PV applications', *IEEE Trans. Ind. Electron.*, 2009, **56**, (11), pp. 4416–4426
- [10] Srinivas, V.L., Kumar, S., Singh, B., *et al.*: 'A multifunctional GPV system using adaptive observer based harmonic cancellation technique', *IEEE Trans. Ind. Electron.*, 2017, *early access*
- [11] Srinivas, V.L., Kumar, S., Singh, B., *et al.*: 'Partially decoupled adaptive filter based multifunctional three phase GPV system', *IEEE Trans. Sust. Energy*, 2017, *early access*
- [12] Singh, M., Khadkikar, V., Chandra, A., *et al.*: 'Grid interconnection of renewable energy sources at the distribution level with power quality improvement features', *IEEE Trans. Power Deliv.*, 2011, **26**, (1), pp. 307–315
- [13] Verma, A.K., Singh, B., Shahani, D.T.: 'Grid interfaced solar photovoltaic power generating system with power quality improvement at AC mains'. *Proc. IEEE Third Int. Conf. Sustainable Energy Technologies (ICSET)*, 2012, pp. 177–182
- [14] Jung, H., Ji, Y., Won, C., *et al.*: 'Improved grid synchronization technique based on adaptive notch filter'. *2010 Int. Power Electronics Conf. (IPEC)*, Sapporo, 2010, pp. 1494–1498
- [15] Singh, B., Jain, C.C., Goel, S.: 'ILST control algorithm of single-stage dual purpose grid connected solar PV system', *IEEE Trans. Power Electron.*, 2014, **29**, (10), pp. 5347–5357
- [16] Agarwal, R., Hussain, I., Singh, B.: 'LMF based control algorithm for single stage three-phase grid integrated solar PV system', *IEEE Trans. Sustain. Energy*, 2016, **7**, (4), pp. 1379–1387
- [17] Karimi-Ghartemani, M., Khajehoddin, S.A., Jain, P.K., *et al.*: 'Addressing DC component in PLL and notch filter algorithms', *IEEE Trans. Power Electron.*, 2012, **27**, (1), pp. 78–86
- [18] IEEE Std. 519-2014: 'IEEE recommended practice and requirements for harmonic control in electric power systems', 2014, pp. 1–29 (revision of IEEE Std. 519-1992)
- [19] Mirbagheri, S.Z., Aldeen, M., Saha, S.: 'A comparative study of MPPT algorithms for standalone PV systems under RCIC'. *Proc. IEEE Int. Conf. Power and Energy Engineering*, 2015
- [20] Zakzouk, N.E., Elsharty, M.A., Abdelsalam, H.A.K., *et al.*: 'Improved performance low-cost incremental conductance PV MPPT technique', *IET Renew. Power Gener.*, 2016, **10**, (4), pp. 561–574

- [21] Kish, G.J., Lee, J.J., Lehn, P.W.: 'Modelling and control of photovoltaic panels utilizing the incremental conductance method for maximum power point tracking', *IET Renew. Power Gener.*, 2012, **6**, (4), pp. 259–266
- [22] Jain, C., Singh, B.: 'Solar energy used for grid connection: a detailed assessment including frequency response and algorithm comparisons for an energy conversion system', *IEEE Ind. Appl. Mag.*, 2017, **23**, (2), pp. 37–50
- [23] Xie, M., Wen, H., Zhu, C., *et al.*: 'DC offset rejection improvement in single-phase SOGI-PLL algorithms: methods review and experimental evaluation', *IEEE Access*, 2017, **5**, pp. 12810–12819
- [24] Singh, B., Chandra, A., Al-Haddad, K.: '*Power quality problems and mitigation techniques*' (John Wiley & Sons Ltd., UK, 2015)
- [25] IEEE Std. 1159-2009: 'IEEE recommended practice for monitoring electric power quality', 26 June 2009, pp. c1–81 (revision of IEEE Std. 1159-1995)